Review

Yael Gutiérrez*, Pablo García-Fernández, Javier Junquera, April S. Brown, Fernando Moreno and Maria Losurdo*

Polymorphic gallium for active resonance tuning in photonic nanostructures: from bulk gallium to two-dimensional (2D) gallenene

https://doi.org/10.1515/nanoph-2020-0314
Received June 4, 2020; accepted July 27, 2020; published online August 10, 2020

Abstract: Reconfigurable plasmonics is driving an extensive quest for active materials that can support a controllable modulation of their optical properties for dynamically tunable plasmonic structures. Here, polymorphic gallium (Ga) is demonstrated to be a very promising candidate for adaptive plasmonics and reconfigurable photonics applications. The Ga *sp*-metal is widely known as a liquid metal at room temperature. In addition to the many other compelling attributes of nanostructured Ga, including minimal oxidation and biocompatibility, its six phases have varying degrees of metallic character, providing a wide gamut of electrical conductivity and optical behavior tunability. Here, the dielectric function of the several Ga phases is introduced and correlated with their respective electronic structures. The key conditions for optimal optical modulation and switching for each Ga phase are evaluated. Additionally, we provide a comparison of Ga with other more common phase-change materials, showing better performance of Ga at optical frequencies. Furthermore, we first report, to the best of our knowledge, the optical properties of liquid Ga in the terahertz (THz) range showing its broad plasmonic tunability from ultraviolet to visible-infrared and down to the THz regime. Finally, we provide both computational and experimental evidence of extension of Ga polymorphism to bidimensional two-dimensional (2D) gallenene, paving the way to new bidimensional reconfigurable plasmonic platforms.

Keywords: active plasmonics; gallenene; gallium; phase-change materials; reconfigurable plasmonics.

***Corresponding authors: Yael Gutiérrez and Maria Losurdo,** Institute of Nanotechnology, CNR-NANOTEC, via Orabona 4, 70126 Bari, Italy, E-mail: gvelay@unican.es (Y. Gutiérrez), maria.losurdo@cnr.it (M. Losurdo). https://orcid.org/0000-0002-1604-7968 (Y. Gutiérrez)
Pablo García-Fernández and Javier Junquera, Departamento de Ciencias de la Tierra y Física de la Materia Condensada, Universidad de Cantabria, Avda. de los Castros s/n, 39005 Santander, Spain
April S. Brown, Department of Electrical and Computer Engineering, Duke University, 27708 Durham, NC, USA
Fernando Moreno, Departamento de Física Aplicada, Universidad de Cantabria, Avda. de los Castros s/n, 39005 Santander, Spain

1 Introduction

Integration of plasmonics in nanophotonic devices has experienced a great progress in recent years owing to the synergy between a better understanding of the fundamental physical mechanisms and the advancements in the synthesis of new materials and device fabrication methodologies. Consequently, development of various passive plasmonic components, such as waveguides, plasmonic crystals, or metamaterials, with tailored photonic properties is facing significant progress. Most of these plasmonic components are based on passive metallic nanostructures, with properties fixed by the nanostructure parameters. Traditional plasmonic metals such as gold (Au) and silver (Ag) have a static plasmonic response showing a lack of reconfigurability, i.e., once the nanostructures are fabricated, their optical characteristics cannot be reversibly modified. Current efforts in plasmonics focus on attaining dynamic functionalities such as tunability, switching, and modulation of electromagnetic waves to develop fully reconfigurable photonic devices with low power consumption, e.g., optical switches and routers, reconfigurable meta-optics, three-dimensional holographic displays, and photonic memories. Therefore, one of the novel frontiers in plasmonics is the blooming *reconfigurable plasmonics* [1–4]. The design and development of active plasmonic switches, modulators, filters, and reconfigurable antennas [5–9] is enabling an ultrafast low-power integrated plasmonic circuit systems that can be controlled electro-optically and ultimately all-optically [10]. Dynamic metasurfaces are promising new platforms for 5G communications, remote sensing, as well as beam steering in Light

detection and ranging (LiDAR) systems, where the insertion of active elements can break the fundamental limitations of passive and static systems.

Tuning, switching, and modulating plasmonic properties in the visible and near-infrared (NIR) range remain major technological challenges driving an extensive quest for active materials that can support a controllable modulation of their optical properties through changes in their structural phase [4, 11–13] and/or composition [14, 15] triggered by external electrical, optical, mechanical, piezoelectric, or chemical stimuli. Phase-change materials (PCMs) are an attractive research topic in photonics and, lately, in plasmonics owing to the dynamic transition of material properties, enabling the development of reconfigurable devices, especially when combined with a plasmonic approach delivering strong field enhancement and localization. Current PCMs investigated in photonics include vanadium dioxide (VO_2), a canonical Mott material with a large refractive index modulation at 1550 nm during the metal-insulator phase transition (MIT) [13, 16, 17], and the chalcogenide family [18]. Chalcogenides are compounds based on the group-16 chalcogen elements (i.e., sulfur [S], selenium [Se], and tellurium [Te]) bound to "network formers" such as antimony (Sb), germanium (Ge), and gallium (Ga). The most well-known chalcogenide compound is $Ge_2Sb_2Te_5$ (GST), which presents a reversible nonvolatile structural phase switching between its crystalline and amorphous phases, entailing a modulation of its optical properties in the NIR. More recently, the chalcogenide stibnite (Sb_2S_3) has been proposed as an alternative to GST for reconfigurable plasmonic devices operating at optical frequencies, presenting its maximum refractive index contrast around 600 nm [12]. However, VO_2 and GST are inherently plagued by their excessive optical losses. Furthermore, GST materials are not plasmonic, and for plasmon reconfigurability, they are generally coupled to a plasmonic metal such as gold or aluminum [19–21]. In the case of VO_2, only its metallic phase is plasmonic, posing an advantage with respect to the GST family by enabling the modulation of the plasmonic response through its MIT [17, 22].

An alternative non-noble plasmonic metal that is flourishing is Ga, which has the peculiarity of being an active phase-transition plasmonic material, i.e., it simultaneously offers a wide polymorphism [11], as shown in Figure 1, and shows an outstanding plasmonic response in a broad spectral range from UV to NIR stable to oxidation [23, 24]. Ga is most commonly known as a nontoxic and biocompatible liquid metal with a melting temperature just higher than the room temperature (T_m = 302.7 K) [25], and it has the advantage of being Complementary metal–oxide–semiconductor (CMOS) compatible.

The inspiring work of Krasavin and Zheludev [5], Bennett et al. [33], and Petropoulos et al. [34] has provided the proof of concept that dynamical control of surface plasmon-polariton signals in metal-on-dielectric waveguides is possible by switching the reversible solid-to-liquid structural phase transition of Ga, as schematized in Figure 2a. They presented a metal (Au) on dielectric (silica) waveguide containing a crystalline α-Ga section with dimensions of a few microns whose structural transformation could be triggered by changes in the temperature or through an external optical excitation. Interestingly, the energy required for high switching contrast for Ga section of 2.5 × 2.5 μm was estimated to be 10 pJ, the switch-on time was reported to be 2–4 ps, and the switch-off time was in the scale of the nanosecond timescales [5]. The reversible light-induced change in the reflectivity of the liquid-/α-Ga system was demonstrated under a wide variety of conditions including different spectral ranges, optical excitation powers and pulse length times, Ga deposition methods, and dielectric material at the interface [33–40]. Optically excited liquid-/α-Ga-silica systems were used in Q-switch fiber lasers over a wide range of wavelengths [41] and were proven to form the basis of cross-wavelength optical switches [42].

The pioneering work of Soares et al. [43] on Ga phase transformations ($\gamma \rightarrow \varepsilon \rightarrow \delta \rightarrow \beta \rightarrow$ liquid) for nanophotonics also envisioned the possibility of using phase change of Ga nanoparticles to create binary and quaternary optical memory elements for nanophotonic systems operating at an extremely low power level [44–46]. The proof of concept of the phase (logic) state of Ga nanoparticle phase-change memory elements was obtained by writing information in the phase state of Ga nanoparticles using electron-beam excitation, while the readout was achieved through measurements of the particles' linear or nonlinear optical properties, such as the change in reflectivity [45] due to the $\gamma \rightarrow \varepsilon \rightarrow \beta \rightarrow$ liquid phase transitions, or in cathodoluminescent emission [47, 48] for the $\beta \rightarrow$ liquid phase transformation on variation of temperature in the range of 90–305 K and of optical excitation average intensities of 160–1260 W/cm^2, as schematized in Figure 2b. In order to get an idea of the data density of those Ga systems [45], one can estimate that building a hexagonal close-packed lattice of 80-nm Ga NPs, the data density is of 0.1 Tb/in^2 for a binary system and 0.2 Tb/in^2 for a quaternary system, assuming that each particle can be individually resolved. For comparison, the data density of a Blue-ray disk is 0.015 Tb/in^2. Concerning the energy requirements, the necessary energy

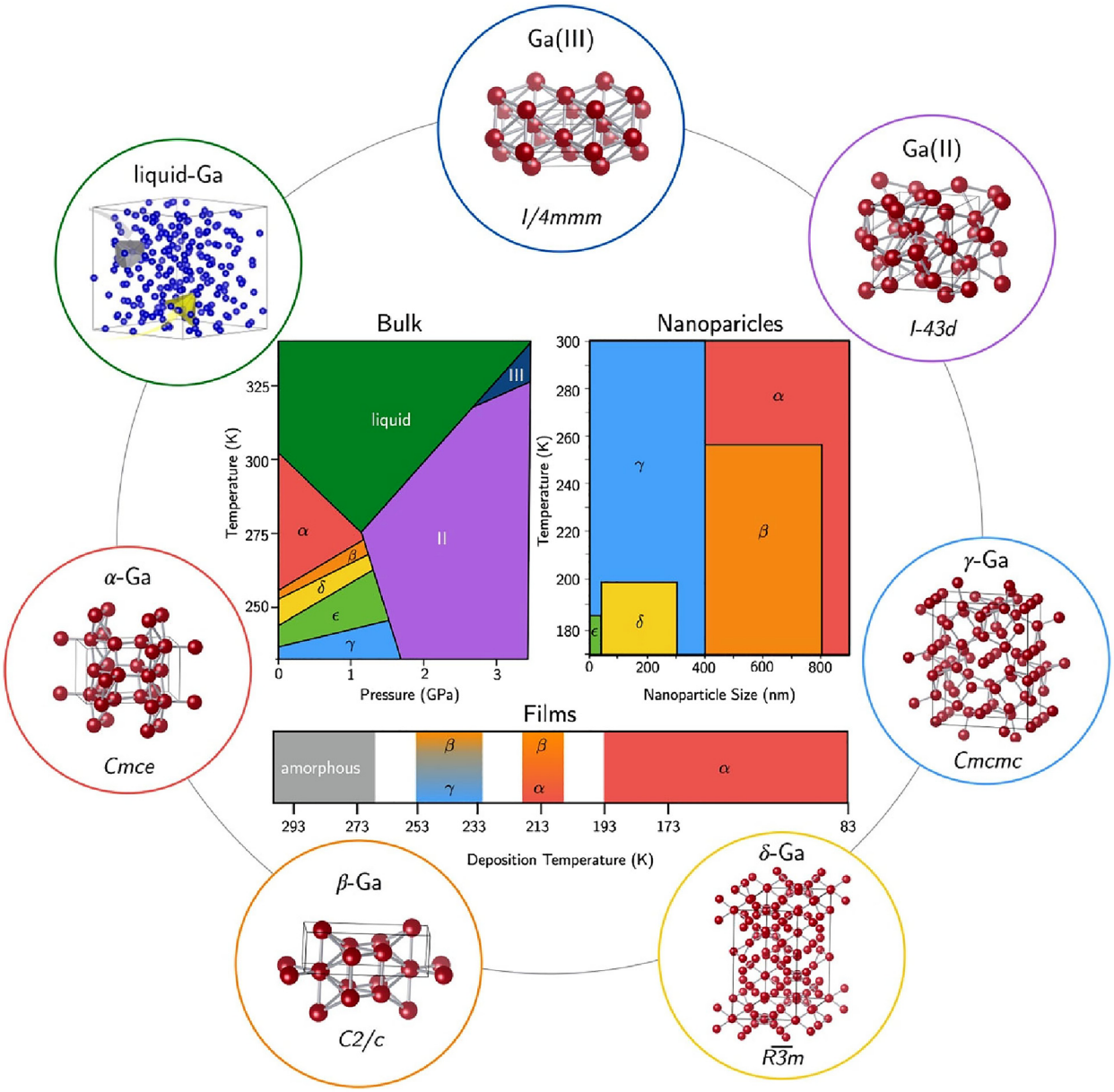

Figure 1: Phase diagram of bulk gallium (Ga) [26] (left) and of Ga nanoparticles [11] (right) as a function of nanoparticle size and scheme of various Ga phases thin films that can be obtained as a function of the deposition temperature [27] (bottom), reconstructed from several referenced sources. The schemes of the different unit cells of each of the crystalline phases are also indicated [26, 28–32].

for phase switching in Ga NPs is 1.5 pJ, lower than state-of-the-art figures of 15 pJ for the energy required to write single bits of information. Therefore, Ga NPs are able to provide low-energy memory functionality–integrated nanophotonic devices. Nevertheless, the full exploitation of Ga phase transitions in reconfigurable plasmonics and nanophotonics has been hampered by the limited knowledge of the optical and plasmonic behavior of the several phases of Ga [49–56]. This has motivated recent works to discuss in depth the electronic, optical, and plasmonic properties of the Ga phases [11, 57], paving the way to a new generation of Ga-based reconfigurable plasmonic structures.

This paper presents recent developments of Ga as a new member of plasmonic PCMs covering a broad spectral range and reviews their implementations in reconfigurable photonic devices. The paper is arranged as follows: Section 2 is devoted to a comprehensive discussion about the electronic structure, optical properties, and their influence on the plasmonic performance of the different bulk Ga phases, focusing on reconfigurable plasmonic

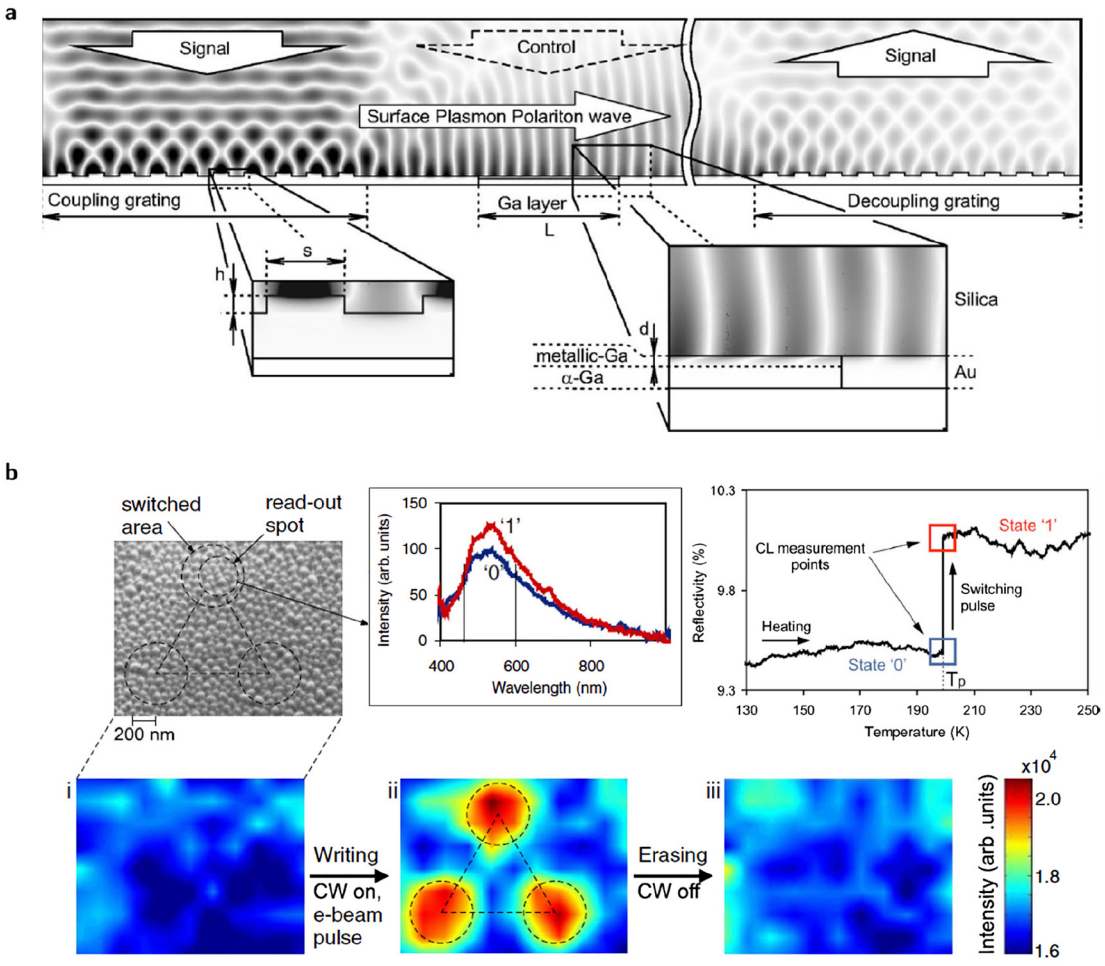

Figure 2: (a) Gold-on-silica surface plasmon polaritons (SPPs) waveguide containing a gallium section used a switch element to control the transmission of the waveguide. Field mapping shows the magnitude of the *z* component of the magnetic field. Rearranged from the study by Krasavin and Zheludev [5]. (b) Gallium particle film reflectivity as a function of increasing temperature, showing abrupt excitation-induced phase memory–state switching at $T = 200$ K. Cathodoluminescence measurements were made immediately before and after the induced transition. Rearranged from the studies by Denisyuk et al. [47, 48].

applications. For the Ga liquid phase, its optical properties down to the terahertz (THz) regime, covering the whole range from THz, VIS to UV are reported for the first time to the best of our knowledge. In Section 3, the potential of Ga as a candidate for the next generation of phase-change plasmonic devices is compared to other PCMs, such as GST, Sb_2S_3, VO_2, and bismuth (Bi), which is another liquid metal emerging for phase-change liquid plasmonics. We introduce the figure-of-merit (FOM) = $\Delta n/\Delta k$, defined as the ratio of the index change to the loss change, to guide the selection of the most suitable Ga phases for high-performance reconfigurable photonics chips at tailored frequencies. Finally, Section 4 demonstrates that Ga polymorphism extends to two-dimensional (2D) level, creating a new class of 2D gallenene switchable PCMs. Details on calculations methods and experimental preparation and characterization of samples are given in Supplementary material.

2 Polymorphism of Ga and the corresponding optical properties

In this section, we review the most important characteristics of bulk Ga, starting with the dielectric function and electronic structure of its different phases. Given this premise, we spectrally analyze the plasmonic performance of each phase in the near-UV, VIS, and NIR spectral ranges. For the liquid phase, extension of experimental measurements to the THz regime for its interest in communication applications is also discussed.

2.1 Electronic structure and dielectric function of Ga phases

Depending on temperature, pressure, and nanostructuring, Ga has been reported to exist in several different phases, as shown in Figure 1, with a different percentage of metallic and covalent Ga bonds that translates into different electronics structures and, consequently, into different optical properties. At low pressure and temperatures $T > 27$ °C, Ga is liquid, while below this temperature, it solidifies in the α-Ga orthorhombic crystal structure that belongs to the *Cmce* (no. 64) space group with eight atoms in the unit cell [32]. Additional metastable Ga phases have been reported with decreasing temperature, i.e., β-Ga with a melting temperature (T_m) of 256.8 K, space group symmetry *C2/c* (no. 15) and eight atoms in the unit [29]; γ-Ga (T_m = 237.6 K) with a complex *Cmcm* (no. 63) structure and 40 atoms/unit cell [31]; ε-Ga (T_m = 244.6 K) whose crystalline structure is still unknown [26]; and δ-Ga (T_m = 253.8 K), which crystallizes in a rhombohedral structure with space group symmetry $R\bar{3}m$ (no. 166) and a unit cell with 22 atoms [30]. Moreover, by increasing pressure, this polymorphism includes also Ga(II) and Ga(III) [26, 57]. Indeed, recently, all those phases have been demonstrated to occur depending on, for instance, the cycles of cooling and heating of the Ga thin film, on deposition methodology of Ga nanoparticles and on their size (see Figure 1), as well as on the epitaxial relationship with the substrate where Ga thin films or nanoparticles are deposited on [11, 24, 27, 58]. As an example, cooling cycles of Ga thin films can result in α-, β-, and γ-Ga [27]. Room temperature ultra high vacuum (UHV) deposition on sapphire and SiC can result in γ-Ga nanoparticles [24], whereas wet deposition methods in solvents of Ga nanoparticles result in the δ-phase [59].

The complex dielectric function, refractive index, and density of states (DOS) of α-Ga, β-Ga, γ-Ga, δ-Ga, and liquid Ga (*l*-Ga) phases are shown in Figure 3. In the case of the solid α-, β-, γ-, and δ-phases, the dielectric function and DOS have been calculated using density functional theory (DFT) methods as described in the study by Gutiérrez et al. [11] and reported in Supplementary material §1. Those calculated spectra were compared to experimental spectra obtained by spectroscopic ellipsometry in the study by Gutiérrez et al. [11]. For the liquid phase, the values of the dielectric function were experimentally measured using spectroscopic ellipsometry in the UV-VIS-NIR and in the THz regime (see experimental details in Supplementary material §2).

The DOS profiles show an increasing metallicity moving from α-Ga (a jagged profile indicating charge localization typical of insulating materials) to δ-Ga (a smooth DOS profile characteristic of metallic delocalized bonds). The DOS of α-Ga presents humps below and above the Fermi energy consistent with two nearly parallel bands associated with bonding-antibonding behavior caused by covalent bonding. Some covalent behavior is also displayed by β-Ga as its DOS also presents broad bands below and above the Fermi energy. However, for β-Ga, the dip between these peaks is less pronounced than for α-Ga, indicating a stronger metallic behavior. γ-Ga shows a smoother DOS like δ-Ga, although the small dip around the Fermi energy is clearly reflected in the imaginary part of the dielectric function. This evolution is clearly observed in the spectra of the complex dielectric function. We can observe in Figure 3 that α-Ga has strong interband transitions at 1050 and 570 nm, which are smoothed in β-Ga at approximately 660 nm, while γ-Ga and δ-Ga display a dispersion profile typical of an ideal Drude metal. Finally, *l*-Ga presents a perfect Drude-like behavior.

Therefore, the following trends of metallic character can be established:

$$l\text{-Ga} > \delta\text{-Ga} > \gamma\text{-Ga} > \beta\text{-Ga} > \alpha\text{-Ga}$$

Interestingly, considering the emerging field of THz plasmonics [60], Figure 3 reports for the first time the dielectric function of *l*-Ga in THz experimentally measured by spectroscopic ellipsometry [61]. The details on the sample preparation and the experimental measurements are available in Supplementary material (§3). In general, it is assumed that the extrapolation of the Drude free-electron model determined at optical frequencies (characterized by the plasma frequency ω_p that lies in the UV frequency range and damping constant Γ—see Supplementary material §4) is a valid description of the dielectric properties of metals across the entire electromagnetic spectrum. By keeping those values, the extrapolation of the Drude model to much lower frequencies (THz) predicts a perfect conductor behavior ($\mathrm{Re}(\varepsilon) \to -\infty$), in general leading to a dielectric function that is orders of magnitude larger than that experimentally measured. Consequently, it is assumed that THz surface plasmons cannot be well confined at the interface, and the perfect conductor Drude extrapolation would imply that devices could only support *spoof surface plasmons* [62]. Indeed, there are several examples in the literature about THz propagating surface plasmons that report them to be more tightly bound than predicted by theory. Moreover, a number of recent measurements of dielectric functions of metals and semiconductors in the THz range showed that they are not consistent with predictions based on the extrapolation of the Drude free-electron model determined at optical frequencies [63–65] (see also Supplementary material §3). Therefore, different

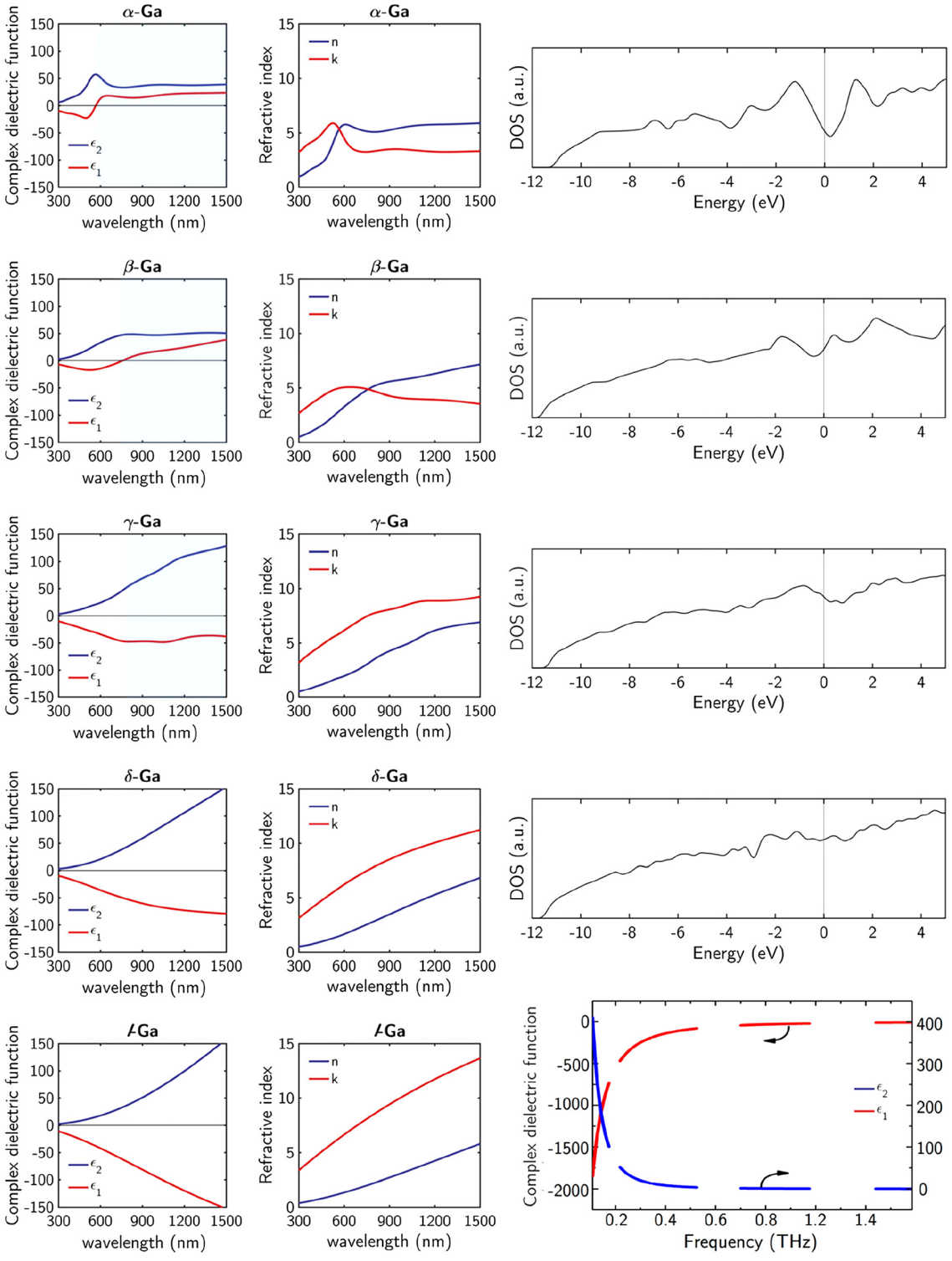

Figure 3: Complex dielectric function ($\varepsilon = \varepsilon_1 + i\varepsilon_2$), complex refractive index ($N = n + ik$), and density of states (DOS) of α-, β-, γ-, and δ-Ga. The experimental complex dielectric function and refractive index of liquid gallium (*l*-Ga) measured by spectroscopic ellipsometry in the UV-NIR and in the THz range is also shown.

modifications to the classical Drude model have been proposed to account for the Drude deviation in the THz range, typically by modifying amplitude oscillator functions to the model dielectric function to effectively reduce the conductivity in those ranges. Indeed, the Drude model constants should be redetermined in the THz range

because both the contributing electron density and effective electron mass are not the same for the high-frequency range (VIS–NIR) and for the low frequency one (THz), and consequently, the plasma frequency and damping constants differ from those obtained for the VIS–NIR range. Ga metal is not an exception to this modification: the Drude extrapolation of *l*-Ga (plasma frequency ω_p = 14.75 eV and damping Γ = 0.85 eV) is plotted in Supplementary material (§4), showing a large discrepancy with the experimental values in Figure 3, hence the importance of experimentally determining the metal *l*-Ga phase dielectric function in the THz regime. The reason for this discrepancy is still under investigation and debate (e.g., effects of surface roughness and/or internal polycrystalline crystal structure of the metal and grain boundaries are being considered among other effects); at the very least, it points out a clear need for theoretical insight into the problem, as well as further measurements (see Supplementary material §3).

2.2 Phase-dependent plasmonic performance of Ga thin films and nanoparticles

The different dielectric functions of the various phases lead to a different optical response in both nanostructured and extended systems. In order to give an overview on the plasmonic performance of the different Ga phases, we have evaluated their corresponding Faraday number (Fa). The Fa, recently proposed by Lalisse et al. [66], is a dimensionless metric that quantifies the ability of a nanoparticle to enhance the electric near-field intensity. Therefore, plasmonic materials able to produce high enhancements of the electromagnetic field are characterized by high values of Fa. Figure 4(a) shows the values of Fa for the Ga phases. It is clear from the plot that the Fa is directly related to the free-electron behavior of Ga phases. Specifically, the γ-, δ-, and *l*-Ga phases with smoothest DOS and Drude-like dielectric function show higher values of the Fa than α- and β-Ga, which have jagged DOS profiles and interband transitions in their dielectric function. Consequently, the localized surface plasmon resonance (LSPR) spectra of Ga nanostructures made of different phases are expected to suffer from a change in amplitude on phase transition. This is the basic principle for realizing Ga nanoparticle–based binary and quaternary optical memory elements [44–46]. To demonstrate this, we have calculated the absorption cross section (C_{abs}) and near-field enhancement ($\langle|\mathbf{E}|^2\rangle$) averaged over the surface of a hemisphere with a radius *R* of 60 nm deposited on a sapphire substrate illuminated under normal incidence, as shown in Figure 4(c,d). The simulated geometry (inset in Figure 4d) has been designed to mimic real Ga samples employed in different types of experiments [24, 67]. The peak appearing in the spectra around 700 nm (in the interband transition regime for α- and β-Ga) corresponds to the longitudinal mode, whereas the increasing values at short wavelengths are related to the transverse mode, which lays deep in the UV and out of the spectral range analyzed here [11]. Clear trends relating C_{abs} and $\langle|\mathbf{E}|^2\rangle$ to

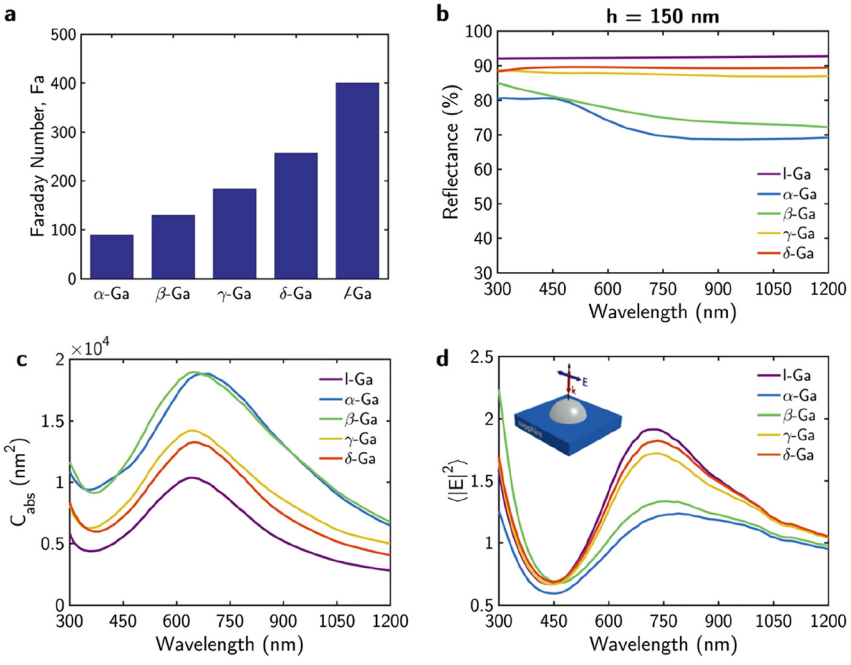

Figure 4: Evaluation of plasmonic performance of thin films and nanostructures. (a) Faraday number (Fa) of the different Ga phases. (b) Reflectance spectra at normal incidence of a 150-nm-thick layer of Ga in the different phases on a sapphire substrate (α-Al_2O_3, n = 1.78). (c) Absorption cross section (C_{abs}) and (d) near-field enhancement ($\langle|\mathbf{E}|^2\rangle$) averaged over the surface of different Ga phase hemispheres of radius R = 60 nm deposited on a sapphire substrate (α-Al_2O_3, n = 1.78) illuminated under normal incidence.

the metallic character of the phases can be seen. On the one hand, C_{abs} decreases as the metallicity of the phases increases. Therefore, both α- and β-Ga show the highest value of C_{abs} caused by their increased absorption owing to interband transitions with respect to those more metallic phases. On the other hand, the inverse trend can be seen for $\langle|\mathbf{E}|^2\rangle$, i.e., $\langle|\mathbf{E}|^2\rangle$ increases with the metallicity of the phase. This trend is consistent with the one shown by the Fa. For instance, γ-, δ-, and *l*-Ga, which have metallic character at 700 nm, show the highest values of $\langle|\mathbf{E}|^2\rangle$ originated by LSPRs. On the contrary, α- and β-Ga at 700 nm are lossy dielectrics, and the resonant peaks can be identified as Mie resonances originated by displacement currents inside the nanoparticle (NP). Near-field enhancements originated through Mie resonances are lower than those generated by LSPRs [68]. This is consistent with the lower values of $\langle|\mathbf{E}|^2\rangle$ for α- and β-Ga as compared to those phases with metallic character (γ-, δ-, and *l*-Ga).

While in applications related to Ga nanoparticle–based binary and quaternary optical memory elements

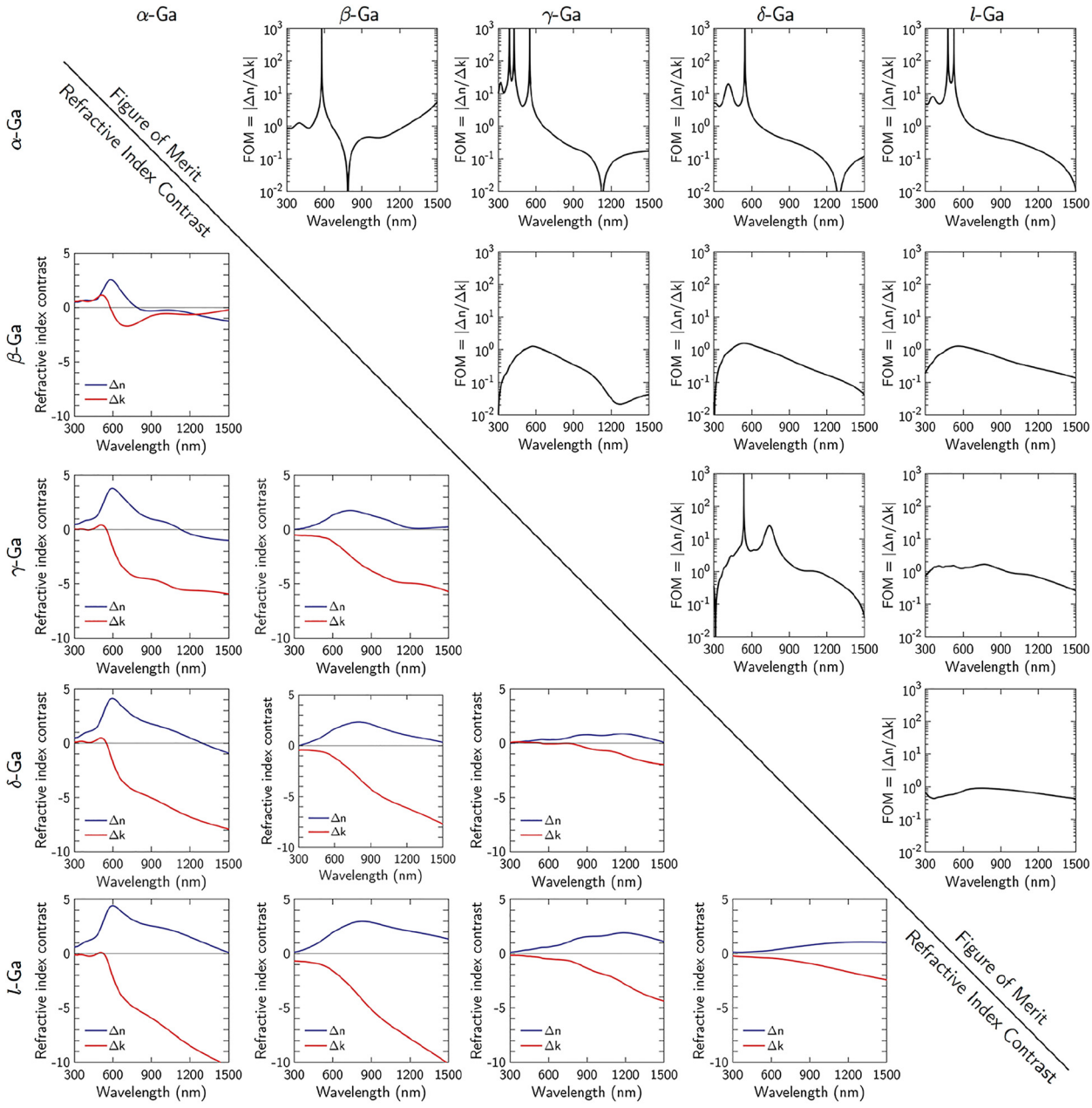

Figure 5: Figure-of-merit (FOM) and refractive index contrast in Ga phase transformations. Combination matrix plot of the FOM = $\Delta n/\Delta k$ (upper diagonal matrix) and refractive index contrast Δn and Δk (down diagonal matrix) on phase transition between Ga phase pairs.

changes in the LSPR amplitude are exploited, other reconfigurable Ga devices rely on the change in reflectivity in Ga thin layers by phase transition [37, 69]. Similarly, for the extended system, we explore the change in reflectivity due to change of the dielectric function by phase transitions, and Figure 4(b) shows the reflectance spectra of a 150-nm-thick Ga phase layer on a sapphire substrate illuminated under normal incidence. As expected, the largest differences in the reflectance spectra of the different Ga phases are produced below ≈620 nm. Those phases with interband transitions below ≈620 nm (i.e., α- and β-Ga) show lower reflectance values because of their dielectric behavior ($\varepsilon_1 > 0$) (this correlates with the fact that when nanostructured, these two phases show the lowest value of the Fa as compared with the other three). Above 620 nm, their reflectance increases because of their metallic behavior ($\varepsilon_1 < 0$). By contrast, those phases with a Drude-like dielectric function (i.e., γ-, δ-, and *l*-Ga) present higher values of reflectance and are almost constant in all the analyzed spectral range. Accordingly, they show the highest values of the Fa when nanostructured.

3 Phase-transitions FOM

3.1 FOM for Ga phase transitions

As pointed out by Abdollahramezani et al. [1], the key condition for optimal optical modulation or switching consists in achieving large changes in the optical constants within the operational spectral region of the device. Ideally, this large change in the optical constants should entail a high contrast in the real part of the refractive index (Δn) with small induced optical losses ($\Delta k \approx 0$) [1]. Therefore, the FOM $\Delta n/\Delta k$ defined as the ratio of the index change to the loss change serves to compare PCMs. In bulk materials, Δn and Δk cannot be independently controlled because the real and imaginary parts of the complex refractive index are Kramers-Kronig related. Consequently, a change in the real part of the refractive index will lead to a change in the imaginary part (and vice versa) in a way that the Kramers-Kronig relation remains preserved.

Therefore, we first compare the FOM = $\Delta n/\Delta k$ between phase transformations in Ga. The combination matrix plot in Figure 5 shows at the upper and lower diagonals the FOM and spectral values of the refractive contrast (i.e., Δn and Δk) calculated for different pairs of Ga phases. The phase transitions involving α-Ga show the highest FOM in the UV-visible range (300–800 nm). Specifically, the α- to β-phase transition shows a pronounce FOM peak, i.e., FOM > 10^3, at 580 nm. Interestingly, the α- to γ-phase transition shows several peaks in the FOM, i.e., three pronounced peaks at 386, 428, and 549 nm and an intermediate intensity (i.e., FOM = 22) at 318 nm. The FOM for the α- to δ-phase transition shows a pronounced peak at 548 nm and an intermediate peak at 410 nm. Finally, the α- to *l*-phase transition shows two pronounced peaks at 480 and 526 nm and an intermediate (i.e., FOM ~ 10) peak at 360 nm. Another interesting transition involving high values of the FOM is the γ- to δ-phase transition, with a pronounced and an intermediate peak at 540 and 743 nm, respectively. All other transitions have poor values of FOM ≤ 1. Figure 6 summarizes the spectral regions where the Ga phase transitions result in the peaks appearing in the FOM evaluated in Figure 5. The size of the dot is related to the value of the FOM at the peak. Therefore, Figure 6 provides a guideline to select the most appropriate Ga phase transition with the highest FOM value depending on the wavelength of interest, mainly in the visible and UV range; only the γ- to δ-Ga phase transition would provide enough optical modulation in the NIR range.

Noteworthily, even for very small values of Δn, if $\Delta k = 0$, an abrupt peak will appear in FOM. Therefore, Figure 7 shows radar plots that gather the values of Δn, Δk, FOM, and wavelength of the main peaks appearing in the FOM spectra. The highest modulation of the refractive index while keeping low losses ($\Delta n > 3$ and $\Delta k = 0$) is produced in the transitions from α- to γ-, α- to δ-, and α- to *l*-Ga at 549, 548, and 526 nm, respectively. The value of Δn for the rest of the peaks ranges between 0.32 and 2.5.

3.2 Phase-transitions FOM in comparison with other PCMs

In order to evaluate the applicability of Ga in phase-change plasmonics and nanophotonics, we compare

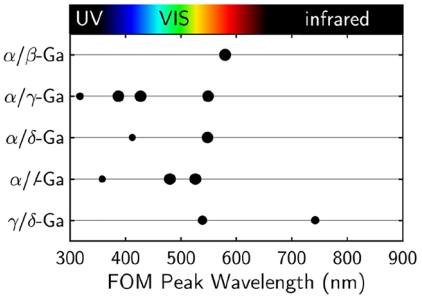

Figure 6: Spectral position of the figure-of-merit (FOM) = $\Delta n/\Delta k$ peaks appearing for different Ga phase transformations. The size of the dot is related to the value of the FOM at the peak.

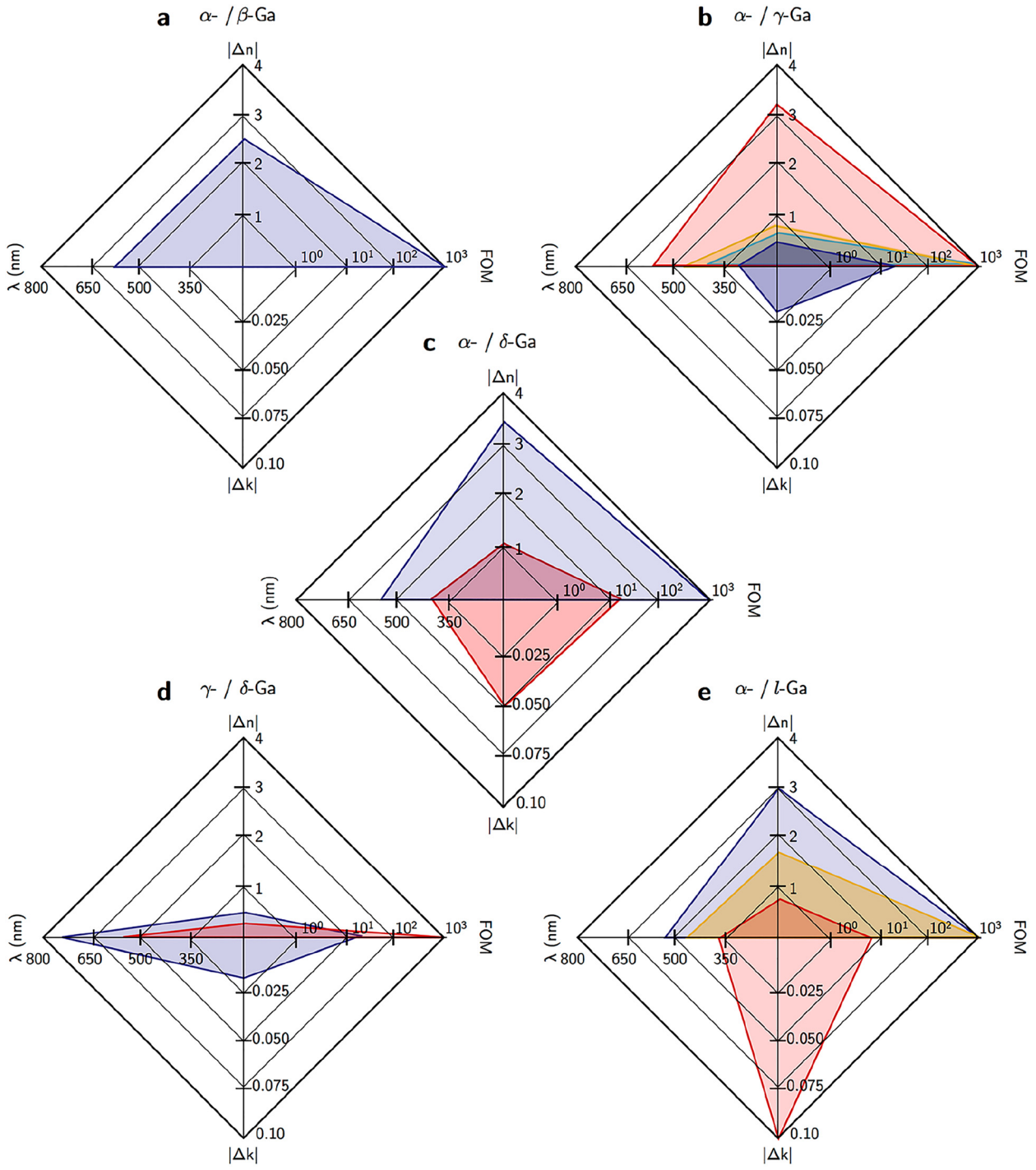

Figure 7: Analysis of the figure-of-merit (FOM) peaks. Radar plots showing the characteristics of the FOM peaks (FOM value, peak wavelength, and refractive index contrast Δn and Δk) appearing in Figure 5 for the transition between (a) alpha-/beta-Ga, (b) alpha-/gamma-Ga, (c) alpha-/delta-Ga, (d) gamma-/delta-Ga and (e) alpha-/liquid-Ga.

the performance of Ga with other four volatile and nonvolatile PCMs under consideration in plasmonics and photonics, characterized by different phase-transition mechanisms:

– *Bi*. Within the selected PCM showcases, Bi is the most similar to Ga. On melting (T_m = 230 °C), Bi undergoes a solid-liquid transition, behaving in its liquid state as a lossy Drude metal [7]. Very recently, Bi NPs embedded

in transparent aluminum oxide metamaterials have been shown to enable the active and analog tuning of the phase of light in the UV-visible spectral range [7].

- *VO_2*. VO_2 undergoes a MIT at a T of 65 °C. On heating, the monoclinic phase is transformed reversibly into the tetragonal phase [13]. On heating across the MIT, optical properties change in the infrared spectral region from a dielectric behavior ($\varepsilon_1 > 0$) to a metallic one ($\varepsilon_1 < 0$) [17]. VO_2 is the most extended volatile PCM.
- *GST*. This chalcogenide PCM is the most extended material for nonvolatile applications such as optical data storage [9]. It has a bandgap tunable in the infrared spectrum from 0.5 to 0.7 eV.
- *Sb_2S_3*. This material of the chalcogenide family has recently been proposed for high-speed reprogrammable photonics devices in the visible spectral range. Unlike other chalcogenide materials such as GST, Sb_2S_3 has a bandgap tunable in the visible spectrum from 1.7 to 2.0 eV. Moreover, the energy barrier of 2.0 eV that separates the amorphous and crystalline phases also enables a nonvolatile behavior [12].

Figure 8 shows the complex dielectric function, $\varepsilon = \varepsilon_1 + i\varepsilon_2$, refractive index contrast, and FOM ($\Delta n/\Delta k$) for the four selected PCM materials. The solid-liquid transition of bismuth shows a sharp peak at 548 nm. VO_2 shows an intense FOM peak at 775 nm, whereas in the infrared spectrum, where VO_2-based devices are proposed to operate [13, 17, 70], the FOM has values between 1 and 0.1. This implies that modulation of the refractive index entails an increase in the optical losses. Similarly, FOM values between 1 and 0.1 characterize GST and Sb_2S_3, in their respective operation spectral ranges, i.e., infrared and visible, respectively. Noteworthily, the α- to β-Ga transition (see the first row in Figure 5) shows in the infrared range above 1200 nm FOM values (between 1 and 10) higher than VO_2 or GST (see FOM in Figure 8).

Although the FOM is a useful parameter for comparing and benchmarking the performance of PCMs, there are additional important parameters to take into account depending on the application. For example, characteristics such as switching time and energies should also be considered. Table 1 shows the switching time, switching energy density, and volatility of the materials considered in this comparison. These values have been extracted from experiments performed on thin films of the considered PCMs in which the phase transformation was induced by optical excitation [5, 12, 71–73]. More information about how the switching energy density has been calculated is available in the Supplementary material §4. The volatile materials (Ga, Bi, and VO_2) show the fastest switching time, with values of the order of picoseconds. Bismuth is the material with fastest switching dynamics (a fraction of picoseconds) [71], followed by Ga (few picoseconds) [5] and VO_2 (tens of picoseconds) [72]. These values of the switching time are orders of magnitude shorter than those of the chalcogenide compounds analyzed here. More precisely, the switching time is of the order of tens of nanoseconds for GST and Sb_2S_3 [12, 73], both nonvolatile PCMs. Considering the energy involved in the phase-change/transition process, VO_2 shows the lowest value of the switching energy density. This value is one order of magnitude lower than that of Ga and Bi and two orders of magnitude lower than those of the chalcogenide compounds. It should be noted that when it comes to systems' energetics, it is also important to consider whether the material is volatile or nonvolatile. For the volatile case, although the switching energy density may be lower than for nonvolatile materials, it needs a continuous energy supply to maintain the switched phase. On the contrary, for nonvolatile materials, once the transformation has occurred, the switched phase will remain without any external energetic supply. So far, many of the reported devices require a steady optical bias to keep their current state, i.e., they are volatile. Although this bias power is negligible in high-rate bit-by-bit switching, it limits the energy consumption in routing schemes where switching occurs at much lower frequencies than the actual data rate [74]. Thus, for such applications, nonvolatile all-optical switches are desirable because they do not continuously consume power (and this can compensate for potentially higher switching energies) [10].

4 Polymorphism in 2D gallenene

The 2D material family has been steadily growing since the disruptive fabrication of graphene [75], and 2D Ga is one of the latest additions to the 2D material family. Very recently, Kochat et al. [76] reported the successful exfoliation of atomically thin layers of Ga on silicon, calling this new form of 2D Ga, gallenene. They introduced two gallenene structures with distinct atomic arrangements, both of them originating from cleavering bulk α-Ga along two different directions, i.e., (010) and (100), the zigzag and honeycomb-like structures. Interestingly, those gallenene forms have been reported to be metallic, thus complementing the semimetallic graphene, semiconducting 2D dichalcogenides, and the insulating 2D h-BN. Other authors have reported the synthesis of ultrathin Ga islands with β-Ga (110) and Ga(III) (010) and (001) structural patterns [77]. Therefore, it seems that the characteristic polymorphism of bulk

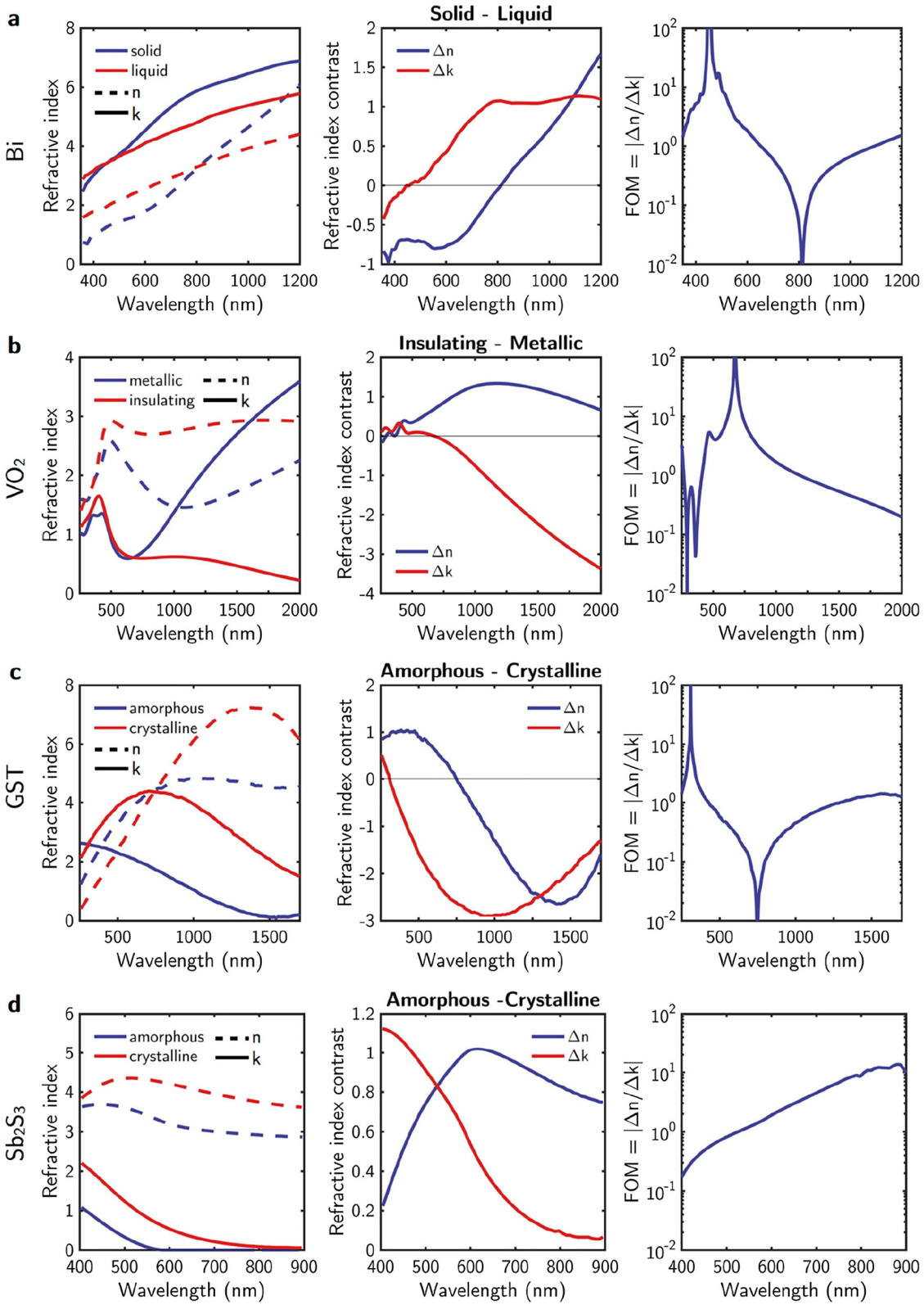

Figure 8: Refractive index ($N = n + ik$), refractive index contrast, and figure-of-merit of common PCMs. Complex dielectric function (first column), refractive index contrast (second column), and FOM = $\Delta n/\Delta k$ (third column) of (a) Bi [7], (b) VO_2 [17], (c) $Ge_2Sb_2Te_5$ (GST) [9], and (d) stibnite (Sb_2S_3) [12]. PCM, phase-change material; VO_2, vanadium dioxide.

Table 1: Switching time, switching energy density, volatility, and bandgap of the considered materials in the comparison.

Material	Switching time (s)	Switching energy density (fJ/nm^3)	Volatile	Nonvolatile
Ga (α–*l*) [5]	$2–4 \times 10^{-12}$	0.0033	Yes	
Bi (solid–liquid) [71]	0.2×10^{-12}	0.0077	Yes	
VO_2 (metal–insulator) [72]	50×10^{-12}	0.0006	Yes	
$Ge_2Sb_2Te_5$ (amorphous–crystalline) [12, 73]	50×10^{-9}	0.031		Yes
Sb_2S_3 (amorphous–crystalline) [12]	80×10^{-9}	0.029		Yes

Ga, gallium; Bi, bismuth; VO_2, vanadium dioxide; Sb_2S_3, stibnite.

Ga prevails also when lowering its dimensionality, envisioning a new generation of 2D phase-change Ga photonic devices.

In order to explore the range of phases of 2D Ga, we have performed DFT simulations of atomically thin layers derived from Ga phases with strongly contrasting optical properties (the computational details are available in Supplementary material §6). α-Ga can be exfoliated along the [001] and [100] directions, as shown in Figure 9a.

Relaxing the exfoliated atomically thin structures, we find three stable 2D Ga allotropes, i.e., the structure extracted from the [001] plane leads to bilayer gallenene (Figure 10a,b), while the [100] direction yields compressed (Figure 10c) and elongated monolayer hexagonal gallenene (Figure 10d). While the bilayer and compressed hexagonal structures have been previously reported in the literature [76, 78, 79], this is, to the best of our knowledge, the first report of the elongated gallenene (Figure 10d). The origin of both compressed and elongated gallenene phases is the cooperative Jahn-Teller effect appearing in the ideal hexagonal phase. Moreover, the elongated gallenene has lower energy (by about 0.24 eV/atom); hence, it should be the phase expected to be experimentally observed if possible stabilizing effect of the substrate is neglected.

From the γ-Ga, we extracted a [001] plane that was subsequently relaxed (see Figure 9b). The obtained stable structure, that we call γ-gallenene (Figure 10e), is the first γ-phase–based 2D Ga structure reported in the literature.

Noteworthily, the final structures originating from relaxation and their stabilization energies are sensitive to

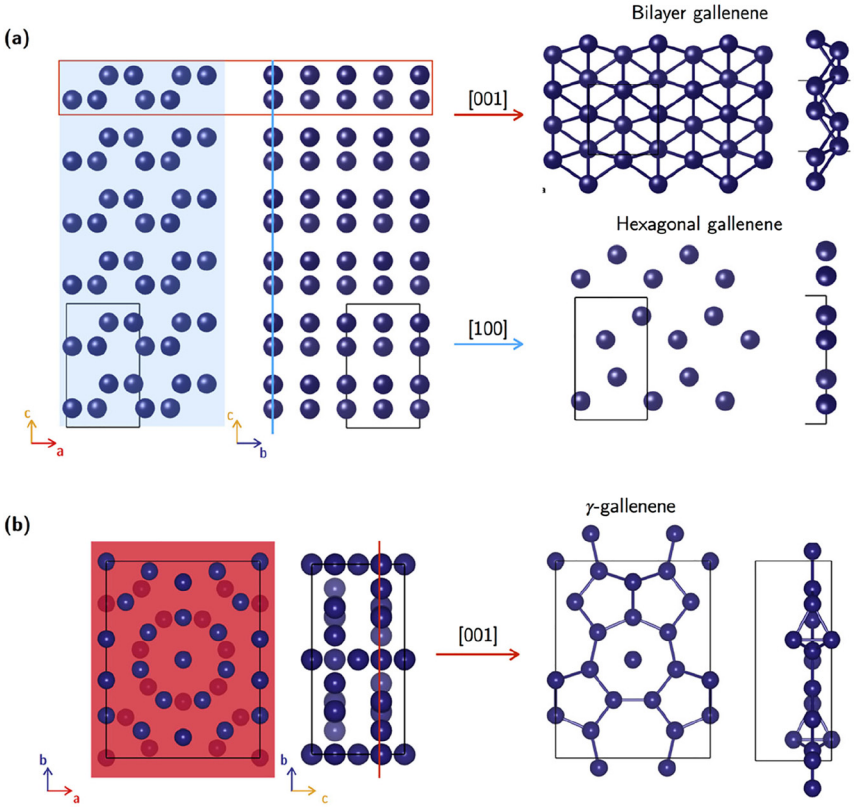

Figure 9: (a) Crystalline structure of α-Ga and its exfoliation along [100] and [001] leading to bilayer and hexagonal 2D gallenene forms. (b) Crystalline γ-Ga and its exfoliation along [001]; the relaxation of this structure leads to γ-gallenene.

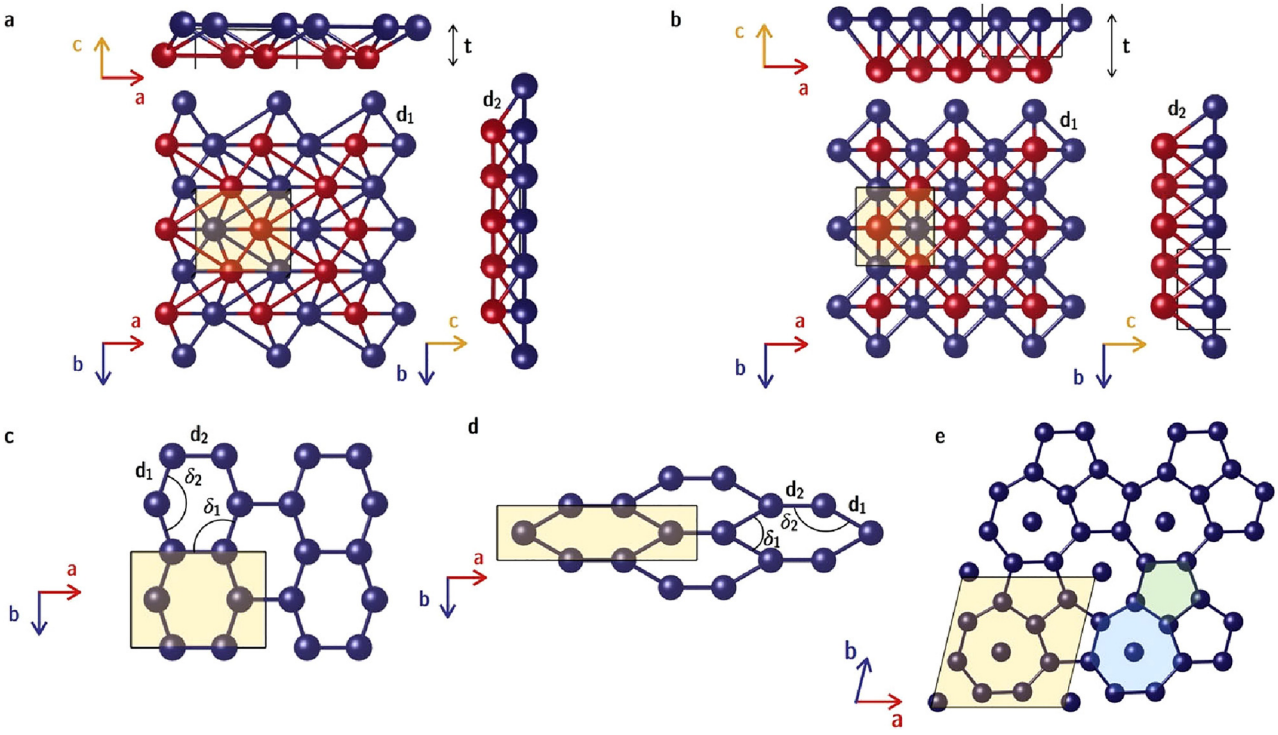

Figure 10: Relaxed structures of the various gallenene phases: (a and b) Perdew–Burke–Ernzerhof (PBE) and PBEsol bilayer gallenene, (c) compressed hexagonal gallenene, (d) elongated hexagonal gallenene, and (e) γ-gallenene. The unit cell is shadowed in yellow. The lattice parameters of each structure are gathered in Supplementary material §7.

the computational technique used. In particular, for bilayer gallenene, Perdew–Burke–Ernzerhof (PBE) [80] or PBEsol [81] (or other similar exchange correlation functionals like WC [82]) leads to significant differences. Specifically, as shown in Figure 10a,b, for bilayer gallenene, the PBE functional leads to a lower symmetry structure than relaxation with PBEsol. However, both functionals predict bilayer gallenene to be the most stable phase and yield the same order for the stability of the higher energy phases, as shown in Table 2. The elongated hexagonal phase has energy very close to bilayer gallenene, i.e., only 0.1 eV/atom by PBE and 0.32 eV/atom by PBEsol higher than bilayer gallenene. γ-gallenene lies in energy above the elongated hexagonal phase, while compressed hexagonal gallenene has energy considerable higher than the previous phases. Thus, several gallenene phases lie in a small energy interval, displaying different symmetries and bond coordination, leading to the conclusion that even in the 2D form, Ga is polymorphic.

Table 2: Relative energy of the different phases of gallenene measured as the total energy per atom as calculated in this work through PBE and PBEsol functionals.

Functional	Bilayer gallenene (eV/atom)	Compressed hexagonal gallenene (eV/atom)	Elongated hexagonal gallenene (eV/atom)	γ-gallenene (eV/atom)
PBE	0.0	0.29	0.10	0.15
PBEsol	0.0	0.56	0.32	0.41

The calculated electronic band structure and DOS of all gallenene structures are detailed in Supplementary material §7. The band calculations reveal that, unlike other 2D monoatomic materials, all 2D Ga allotropes are metallic, with many bands crossing the Fermi energy. However, the jagged profile of the DOS of the bilayer and compressed hexagonal phases indicate some degree of charge localization. Based on these band structures and the dipolar transition matrix elements between occupied and unoccupied single-electron eigenstates, the in-plane and out-of-plane complex dielectric function is calculated for the different phases using first-order time-dependent perturbation theory as implemented in SIESTA [83] and shown in Figure 11. It can be observed that the in-plane γ-gallenene has a completely metallic behavior in-plane with a rather featureless quick decay in the dielectric constant, whereas all other phases show a characteristic sharp interband absorption peak in the 1.7–2.6 eV range.

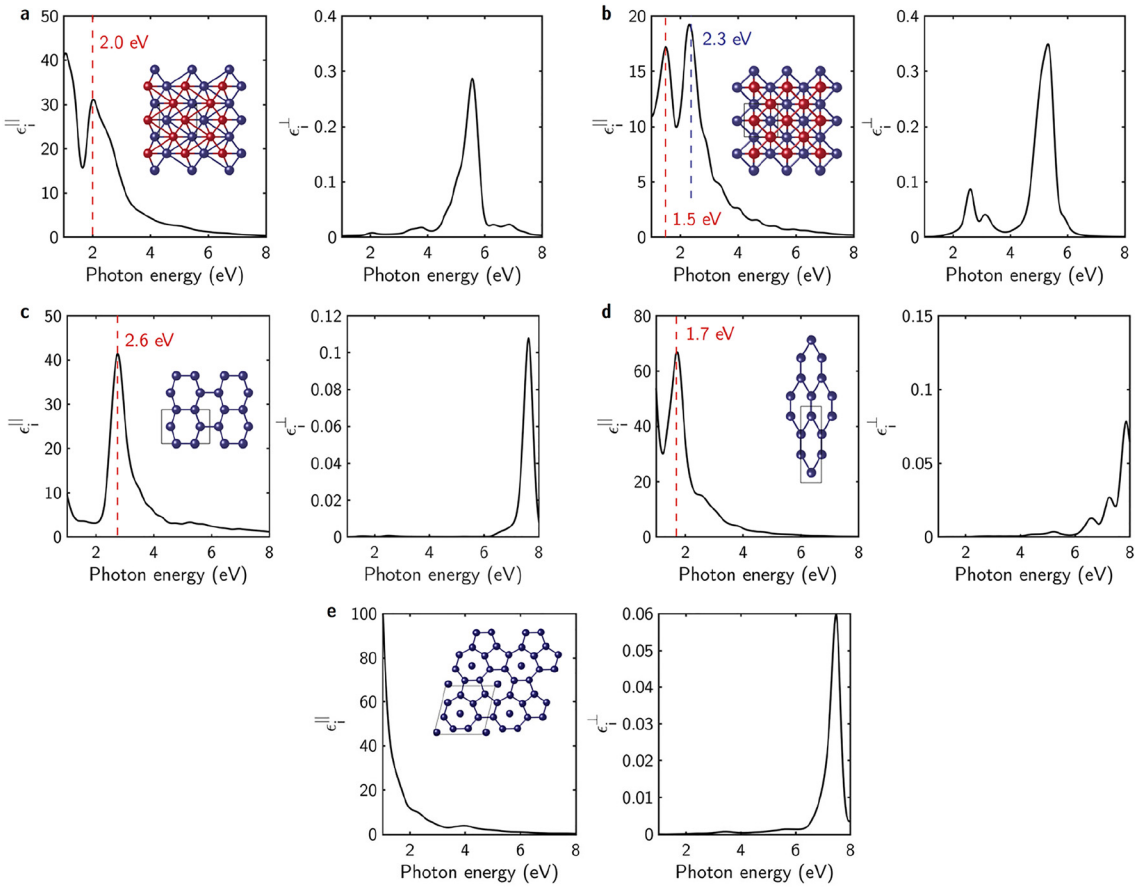

Figure 11: Imaginary part of in-plane ($\varepsilon_i^{\parallel}$) and out-of-plane ($\varepsilon_i^{\perp}$) dielectric function of the different gallenene phases: (a and b) PBE and PBEsol bilayer gallenene, (c) compressed hexagonal gallenene, (d) elongated hexagonal gallenene, and (e) γ-gallenene.

Therefore, similar to bulk Ga, 2D gallenene displays a rich phase diagram with many close-in-energy allotropes. We envisage that experimentally stabilization of each of those various phases could be achieved through interaction with different substrates, where the 2D Ga layer could be deposited. Moreover, Figure 10 shows that compressed/elongated gallenene phases involve strained phases of the ideal hexagonal crystal along the *x*- or *y*-directions. Therefore, growing this phase on a piezoelectric substrate may allow switching from one to the other, this change being accompanied by a large shift of the main absorption peak from 1.7 to 2.6 eV in compressed and elongated gallenene, respectively. This concept is illustrated in Figure 12 that shows the calculated normal incidence reflectance (R) and absorbance (A) spectra of a monolayer of compressed and elongated hexagonal gallenene on a sapphire substrate. The calculations have been performed using the full 2D model proposed by Li and Heinz [84]. On phase transition, the following modulation of reflectance and absorbance can be achieved ΔA (1.7 eV) = 4.6%, ΔA (2.6 eV) = 4.6%, ΔR (1.7 eV) = 1.8%, and ΔR (2.6 eV) = 1.3%.

As proof of concept of the 2D polymorphism in gallenene, we have made first attempts to obtain gallenene sheets and flakes on Si/SiO_2 and Al_2O_3 substrates as well as on graphene using the solid-melt exfoliation by Ga liquid droplets [76]. Stabilized bilayer gallenene on the (0001) plane of gallium nitride (GaN) was obtained by molecular beam epitaxy [85] (details on fabrication and characterization methodologies of gallenene are in Supplementary material §5). The main experimental results are summarized in Figure 13. Optical images of large gallenene-covered areas are well seen on Si/SiO_2 (see Figure 13a), on Al_2O_3 (see Figure 13b), on monolayer graphene (Figure 13c), and on GaN(0001) (Figure 13d) substrates by the optical contrast micrographs. The atomic force microscopy profile analysis showed a thickness of the flakes of approximately 3 nm on Al_2O_3 and Si/SiO_2 substrates. Conversely, the heteroepitaxial Ga layer on GaN(0001) by Molecular Beam Epitaxy (MBE) had a thickness of approximately 5 Å (as estimated by the analysis of spectroscopic ellipsometry spectra acquired before and after Ga deposition on GaN operated in situ to avoid any

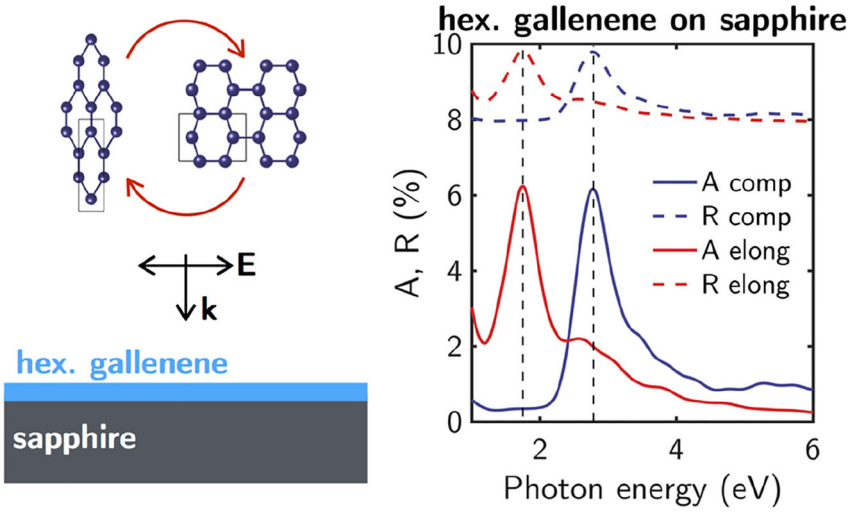

Figure 12: Absorbance (*A*, solid line) and reflectance (*R*, solid line) spectra of a monolayer of compressed (comp-blue) and elongated (elong-red) hexagonal gallenene.

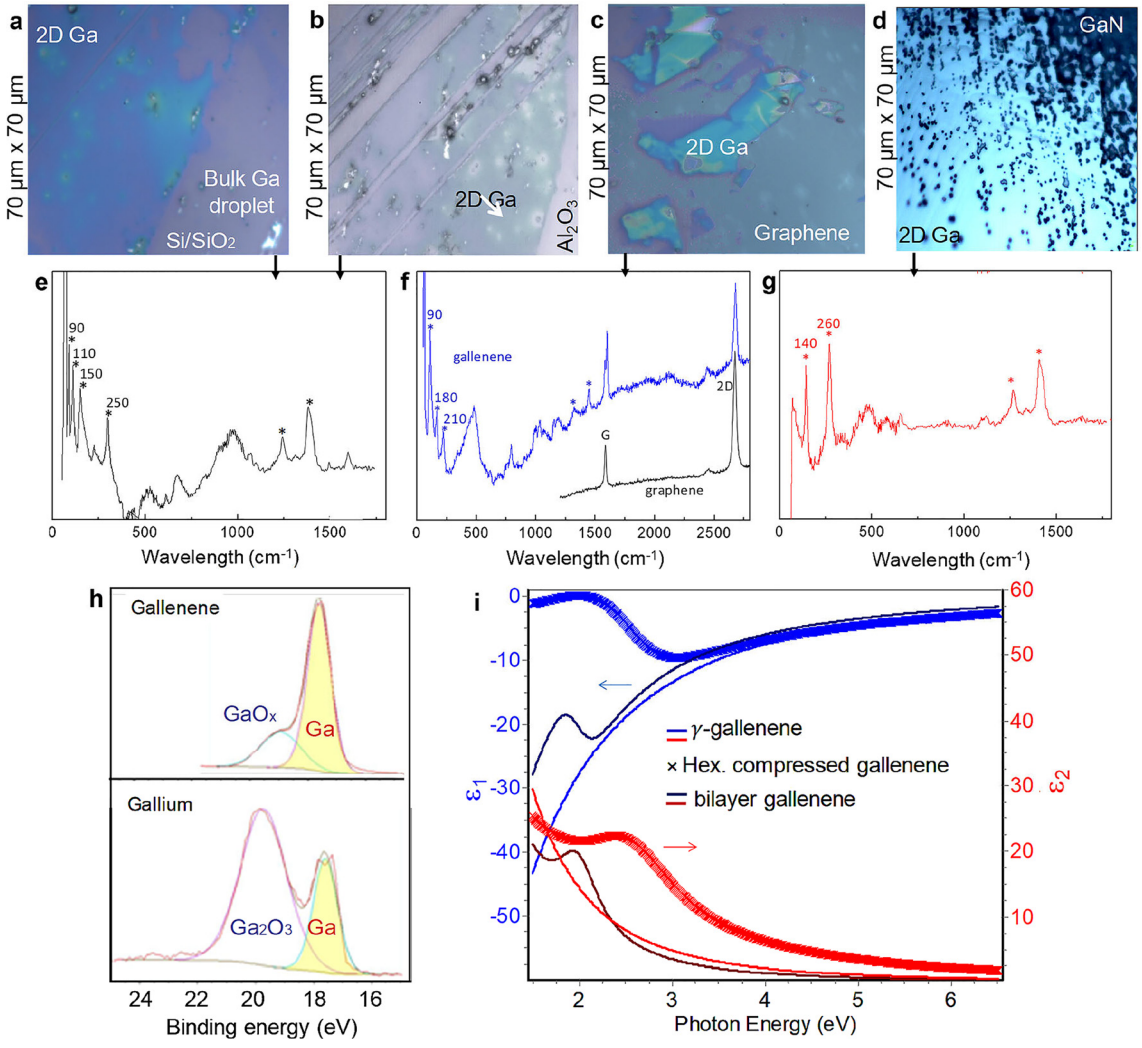

Figure 13: Optical micrographs of two-dimensional (2D) gallenene on (a) Si/SiO_2, (b) Al_2O_3, (c) graphene, and (d) GaN(0001) substrates; (a–c) were obtained by the solid-melt exfoliation technique [76], whereas (d) was obtained by Molecular Beam Epitaxy (MBE). Confocal micro-Raman spectra of gallenene lattices exfoliated onto (e) Si/SiO_2 and Al_2O_3 and (f) graphene and (g) grown by MBE on GaN(0001). (h) Comparison of the XPS spectra of the Ga3d photoelectron peak for gallium and gallenene. (i) Dielectric function experimentally determined by ellipsometry of hexagonal compressed gallenene on sapphire, of bilayer gallenene on GaN(0001), and of γ-gallenene on graphene.

contamination). This value is consistent with a Ga bilayer considering that the shortest Ga-Ga distance in α-Ga is 2.39 Å.

Confocal micro-Raman spectroscopy and X-ray photoelectron spectroscopy (XPS) have been used to characterize the 2D gallenene samples (details are in Supplementary material §5). Specifically, after subtraction of the corresponding substrates' Raman peaks, four Raman bands at approximately 90, 110, 150, and 250 cm^{-1} are visible in the Raman spectra of gallenene on Si/SiO_2 and Al_2O_3. These bands can be assigned to the modes B2g (2×) and B3g of solid α-Ga and correspond to the shortest Ga-Ga distance in hexagonal compressed gallenene, indicating the formation of hexagonal compressed gallenene on Si/SiO_2 and Al_2O_3 substrates. Conversely, the bands at approximately 90, 180, and 210 cm^{-1} characteristic of γ-gallenene appear for gallenene formed by solid-melt exfoliation on graphene, paving the way of forming gallenene/graphene 2D van der Waals heterostructures. The Raman bands at 140 and 260 cm^{-1} characterize bilayer gallenene on GaN(0001). In the region above 1300 cm^{-1}, the Raman spectra of gallenene exhibit characteristic peaks of the hexagonal ring arrangement, with the E2g phonon modes at approximately ≈1320 and ≈1450 cm^{-1} analogous to the E2g mode of 2D BN and of graphene. Interestingly, XPS indicates the stabilization of gallenene because the comparison of the Ga3d photoelectron peak for bulk Ga and gallenene indicates less oxidation (to a suboxide) for the gallenene layer compared to bulk Ga. This verified gallenene stability is consistent with recent work by Steenbergen and Gaston [86].

Microellipsometry has been used to measure, for the first time to the best of our knowledge, the optical spectra of epitaxial bilayer gallenene on the GaN(0001) and of the exfoliated hexagonal gallenene on Al_2O_3 substrate and grapheme, as shown in Figure 13i. To derive those optical data, we first measured the optical spectrum of the substrate, and then, we measured that of substrate + gallenene. After that, a point-by-point fit subtracting the substrate contribution was operated in the simple substrate + gallenene layer assumption. Noteworthily, as in the case of Raman spectroscopy, spectroscopic ellipsometry also give indication of gallenene polymorphism. The comparison of the ellipsometric spectra with the calculated dielectric function indicates that a compressed gallenene is formed on Si/SiO_2 and Al_2O_3 resembling α-Ga as indicated by the peak at approximately 2.5 eV. Bilayer gallenene on GaN(0001) is consistent with the broad interband absorption peak at approximately 2 eV. Conversely, a more metallic dielectric function is measured for the gallenene on graphene resembling γ-Ga, also consistently with the Raman measurements.

5 Summary and outlook

To summarize, we have provided a glimpse of the dynamic optical behavior of phase-change Ga-based structures, including the fundamental optical properties of Ga phases from bulk to the newborn 2D polymorphic gallenene. For the latter, we report the first computational and experimental values of the dielectric function for several phases. The comparison of Ga with some more common, i.e., VO_2 and GST, and emerging, i.e., Bi and Sb_2S_3, PCMs indicates superior performance of Ga for phase-change plasmonics at optical frequencies. Although the application of phase-change plasmonic structures is still in its infancy, the progress enabled by a deeper knowledge of the optical properties of the various phases, and a better understanding of the experimental and technological parameters controlling the different phases, including the impact of the material dimensionality on phases, is encouraging. Therefore, we are witnessing the expansion of the exciting field of active reconfigurable matter, aimed at controlling the phase transitions by external stimuli. Moreover, while PCMs currently operate at telecom wavelength, PCMs at optical wavelengths are emerging. Furthermore, there is a need to extend phase-change devices to the THz regime; hence, we have provided, for the first time to the best of our knowledge, the optical properties of *l*-Ga down to the THz regime. We demonstrate deviation of the experimentally determined optical constant from the Drude model extrapolation, an approximation widely spread in the literature. This emphasizes also the relevance of developing reliable THz spectroscopies for optical databases to drive the accurate design of THz devices.

Furthermore, we also envisage a few promising future directions to make phase-change plasmonic systems becoming a widely deployable technology. Reconfigurability in phase-change plasmonic materials, capable of self-reconfiguring and self-adapting as a response to light, will open up a new chapter in extreme light-matter interactions in a novel class of nanostructured and bidimensional systems wherein phase-change dynamics might not be volume dependent but topological state dependent and that their effect on the electronic and optical properties have to be yet defined. The exciting outcomes might also include demonstrations of future developments of self-responding intelligent photonic systems, ultrafast and low-power switches, adaptive antennas, and adaptive wavelength routing. In all those envisaged applications, the Ga structures' CMOS compatibility with silicon photonics components is a significant advantage for such a success.

Acknowledgments: This work has been supported by the European Union's Horizon 2020 research and innovation program under grant agreement no. 899598 – PHEMTRONICS. F.M. acknowledges MICINN (Spanish Ministry of Science and Innovation) through project PGC2018-096649-B-100. M.L. also acknowledges the cooperation of Prof. Nikolas J. Podraza, Prof. Robert Collins, and Dr. Maxwell Junda at the University of Toledo for making their THz ellipsometer and expertise available for running the THz ellipsometric measurements.

Author contribution: All the authors have accepted responsibility for the entire content of this submitted manuscript and approved submission.

Research funding: This work has been supported by the European Union's Horizon 2020 research and innovation program under grant agreement no. 899598 – PHEMTRONICS. F.M. acknowledges MICINN (Spanish Ministry of Science and Innovation) through project PGC2018- 096649-B-100. M.L. also acknowledges the cooperation of Prof. Nikolas J. Podraza, Prof. Robert Collins, and Dr. Maxwell Junda at the University of Toledo for making their THz ellipsometer and expertise available for running the THz ellipsometric measurements.

Conflict of interest statement: The authors declare no conflicts of interest regarding this article.

References

[1] S. Abdollahramezani, O. Hemmatyar, H. Taghinejad, et al., "Tunable nanophotonics enabled by chalcogenide phase-change materials," *Nanophotonics*, vol. 9, pp. 1189–1241, 2020.

[2] T. Jostmeier, J. Zimmer, H. Karl, H. J. Krenner, and M. Betz, "Optically imprinted reconfigurable photonic elements in a VO_2 nanocomposite," *Appl. Phys. Lett.*, vol. 105, 2014, Art no. 071107.

[3] M. R. Hashemi, S. Cakmakyapan, and M. Jarrahi, "Reconfigurable metamaterials for terahertz wave manipulation," *Rep. Prog. Phys.*, vol. 80, 2017, Art no. 094501.

[4] M. Wuttig, H. Bhaskaran, and T. Taubner, "Phase-change materials for non-volatile photonic applications," *Nat. Photonics*, vol. 11, pp. 465–476, 2017.

[5] A. V. Krasavin and N. I. Zheludev, "Active plasmonics: controlling signals in Au/Ga waveguide using nanoscale structural transformations," *Appl. Phys. Lett.*, vol. 84, pp. 1416–1418, 2004.

[6] S. R. C. Vivekchand, C. J. Engel, S. M. Lubin, et al., "Liquid plasmonics manipulating surface plasmon polaritons via phase transitions," *Nano Lett.*, vol. 12, pp. 4324–4328, 2012.

[7] M. Garcia-Pardo, E. Nieto-Pinero, A. K. Petford-Long, R. Serna, and J. Toudert, "Active analog tuning of the phase of light in the visible regime by bismuth-based metamaterials," *Nanophotonics*, vol. 9, pp. 885–896, 2020.

[8] M. Wuttig and N. Yamada, "Phase-change materials for rewriteable data storage," *Nat. Mater.*, vol. 6, pp. 824–832, 2007.

[9] W. H. P. Pernice and H. Bhaskaran, "Photonic non-volatile memories using phase change materials," *Appl. Phys. Lett.*, vol. 101, p. 171101, 2012.

[10] M. Stegmaier, C. Ríos, H Bhaskaran, C. D. Wright, and W. H. P. Pernice, "Nonvolatile all-optical 1×2 switch for chipscale photonic networks," *Adv. Opt. Mater.*, vol. 5, p. 1600346, 2017.

[11] Y. Gutiérrez, M. Losurdo, P. García-Fernández, et al., "Gallium polymorphs: phase-dependent plasmonics," *Adv. Opt. Mater.*, vol. 7, p. 1900307, 2019.

[12] W. Dong, H. Liu, J. K. Behera, et al., "Wide bandgap phase change material tuned visible photonics," *Adv. Funct. Mater.*, vol. 29, p. 1806181, 2019.

[13] Y. Ke, S. Wang, G. Liu, M. Li, T. J. White, and Y. Long, "Vanadium dioxide: the multistimuli responsive material and its applications," *Small*, vol. 14, p. 1802025, 2018.

[14] G. B. Smith, D. Golestan, and A. R. Gentle, "The insulator to correlated metal phase transition in molybdenum oxides," *Appl. Phys. Lett.*, vol. 103, 2013, Art no. 051119.

[15] J. Meng, Z. Fu, M. Du, X. Liu, and L. Hao, "Influence of ion–atom arrival ratio on structure and optical properties of ZrN x films," *Mater. Lett.*, vol. 164, pp. 291–293, 2016.

[16] M. Sun, M. Taha, S. Walia, et al., "A photonic switch based on a hybrid combination of metallic nanoholes and phase-change vanadium dioxide," *Sci. Rep.*, vol. 8, p. 11106, 2018.

[17] J. John, Y. Gutierrez, Z. Zhang, et al., "Multipolar resonances with designer tunability using VO_2 phase-change materials," *Phys. Rev. Appl.*, vol. 13, 2020, Art no. 044053.

[18] F. Ding, Y. Yang, and S. I. Bozhevolnyi, "Dynamic metasurfaces using phase-change chalcogenides," *Adv. Opt. Mater.*, vol. 7, p. 1801709, 2019.

[19] N. Kumar, A. Rúa, J. Aldama, K. Echeverría, F. E. Fernández, and S. Lysenko, "Photoinduced surface plasmon switching at VO_2/Au interface," *Opt. Express*, vol. 26, p. 13773, 2018.

[20] M. B. Cortie, A. Dowd, N. Harris, and M. J. Ford, "Core-shell nanoparticles with self-regulating plasmonic functionality," *Phys. Rev. B*, vol. 75, p. 113405, 2007.

[21] A. Tittl, A.-K. U. Michel, M. Schäferling, et al., "A switchable mid-infrared plasmonic perfect absorber with multispectral thermal imaging capability," *Adv. Mater.*, vol. 27, pp. 4597–4603, 2015.

[22] L. Wang, E. Radue, S. Kittiwatanakul, et al., "Surface plasmon polaritons in VO_2 thin films for tunable low-loss plasmonic applications," *Opt. Lett.*, vol. 37, p. 4335, 2012.

[23] P. C. Wu, M. Losurdo, T.-H. Kim, S. Choi, G. Bruno, and A. S. Brown, "In situ spectroscopic ellipsometry to monitor surface plasmon resonant group-III metals deposited by molecular beam epitaxy," *J. Vac. Sci. Technol. B Microelectron. Nanometer Struct.*, vol. 25, p. 1019, 2007.

[24] M. Losurdo, A. Suvorova, S. Rubanov, K. Hingerl, and A. S. Brown, "Thermally stable coexistence of liquid and solid phases in gallium nanoparticles," *Nat. Mater.*, vol. 15, pp. 995–1002, 2016.

[25] H. Song, T. Kim, S. Kang, H. Jin, K. Lee, and H. J. Yoon, "Ga-Based liquid metal micro/nanoparticles: recent advances and applications," *Small*, vol. 16, p. 1903391, 2020.

[26] L. Bosio, "Crystal structures of Ga(II) and Ga(III)," *J. Chem. Phys.*, vol. 68, pp. 1221–1223, 1978.

[27] D. Fischer, B. Andriyevsky, and J. C. Schön, "Systematics of the allotrope formation in elemental gallium films," *Mater. Res. Express*, vol. 6, p. 116401, 2019.
[28] F. Zhang, Y. Sun, X. D. Wang, et al., "Structural connection between gallium crystals and near-T m liquids under ambient pressure," *Scr. Mater.*, vol. 143, pp. 86–89, 2018.
[29] L. Bosio, A. Defrain, H. Curien, and A. Rimsky, "Structure cristalline du gallium β," *Acta Crystallogr. Sect. B Struct. Crystallogr. Cryst. Chem.*, vol. 25, p. 995, 1969.
[30] L. Bosio, H. Curien, M. Dupont, and A. Rimsky, "Structure cristalline de Gaδ," *Acta Crystallogr. Sect. B Struct. Crystallogr. Cryst. Chem.*, vol. 29, pp. 367–368, 1973.
[31] L. Bosio, H. Curien, M. Dupont, and A. Rimsky, "Structure cristalline de Gaγ," *Acta Crystallogr. Sect. B Struct. Crystallogr. Cryst. Chem.*, vol. 28, p. 1974, 1972.
[32] J. Zemann, "Crystal structures, 2nd edition. Vol. 1 by R. W. G. Wyckoff," *Acta Crystallogr.*, vol. 18, p. 139, 1965.
[33] P. J. Bennett, S. Dhanjal, P. Petropoulos, D. J. Richardson, N. I. Zheludev, and V. I. Emelyanov, "A photonic switch based on a gigantic, reversible optical nonlinearity of liquefying gallium," *Appl. Phys. Lett.*, vol. 73, pp. 1787–1789, 1998.
[34] P. Petropoulos, H. S. Kim, D. J. Richardson, V. A. Fedotov, and N. I. Zheludev, "Light-induced metallization at the gallium-silica interface," *Phys. Rev. B*, vol. 64, p. 193312, 2001.
[35] V. Albanis, R. T. Bratfalean, S. Dhanjal, et al., "Light-induced specular-reflectivity suppression at a gallium/silica interface," *Opt. Lett.*, vol. 25, p. 1594, 2000.
[36] K. F. MacDonald, V. A. Fedotov, R. W. Eason, et al., "Light-induced metallization in laser-deposited gallium films," *J. Opt. Soc. Am. B*, vol. 18, p. 331, 2001.
[37] V. Albanis, S. Dhanjal, V. A. Fedotov, et al., "Nanosecond dynamics of a gallium mirror's light-induced reflectivity change," *Phys. Rev. B*, vol. 63, p. 165207, 2001.
[38] A. V. Rode, M. Samoc, B. Luther-Davies, E. G. Gamaly, K. F. MacDonald, and N. I. Zheludev, "Dynamics of light-induced reflectivity switching in gallium films deposited on silica by pulsed laser ablation," *Opt. Lett.*, vol. 26, p. 441, 2001.
[39] V. Albanis, V. A. Fedotov, and N. I. Zheludev, "Light-induced reflectivity switching in gallium-on-silica films in the blue–green spectral region," *Opt. Commun.*, vol. 214, pp. 271–276, 2002.
[40] M. Woodford, K. F. MacDonald, G. C. Stevens, and N. I. Zheludev, "Optical switching at ZnSe–Ga interfaces via nanoscale light-induced metallisation," *Opt. Commun.*, vol. 254, pp. 340–343, 2005.
[41] P. Petropoulos, H. L. Offerhaus, D. J. Richardson, S. Dhanjal, and N. I. Zheludev, "Passive Q-switching of fiber lasers using a broadband liquefying gallium mirror," *Appl. Phys. Lett.*, vol. 74, pp. 3619–3621, 1999.
[42] V. Albanis, S. Dhanjal, N. Zheludev, P. Petropoulos, and D. Richardson, "Cross-wavelength all-optical switching using nonlinearity of liquefying gallium," *Opt. Express*, vol. 5, p. 157, 1999.
[43] B. F. Soares, K. F. MacDonald, V. A. Fedotov, and N. I. Zheludev, "Light-induced switching between structural forms with different optical properties in a single gallium nanoparticulate," *Nano Lett.*, vol. 5, pp. 2104–2107, 2005.
[44] A. I. Denisyuk, F. Jonsson, and N. I. Zheludev, "Phase-change memory functionality in gallium nanoparticles," in *2007 Eur. Conf. Lasers Electro-Optics Int. Quantum Electron. Conf.*, *IEEE*, 2007, p. 1.
[45] B. F. Soares, F. Jonsson, and N. I. Zheludev, "All-optical phase-change memory in a single gallium nanoparticle," *Phys. Rev. Lett.*, vol. 98, pp. 1–4, 2007.
[46] N. I. Zheludev, "Single nanoparticle as photonic switch and optical memory element," *J. Opt. A Pure Appl. Opt.*, vol. 8, pp. S1–S8, 2006.
[47] A. I. Denisyuk, F. Jonsson, K. F. MacDonald, N. I. Zheludev, and F. J. García de Abajo, "Luminescence readout of nanoparticle phase state," *Appl. Phys. Lett.*, vol. 92, 2008, Art no. 093112.
[48] A. I. Denisyuk, K. F. MacDonald, F. J. García de Abajo, and N. I. Zheludev, "Towards femtojoule nanoparticle phase-change memory," *Jpn. J. Appl. Phys.*, vol. 48, 2009, Art no. 03A065.
[49] G. Jezequel, J. C. Lemonnier, and J. Thomas, "Optical properties of gallium films between 2 and 15 eV," *J. Phys. F Met. Phys.*, vol. 7, pp. 1613–1622, 1977.
[50] A. P. Lenham, "The optical constants of gallium," *Proc. Phys. Soc.*, vol. 82, pp. 933–937, 1963.
[51] O. Hunderi and R. Ryberg, "Band structure and optical properties of gallium," *J. Phys. F Met. Phys.*, vol. 4, pp. 2084–2095, 1974.
[52] O. Hunderi, "The band structure in monoclinic β-Ga," *J. Phys. F Met. Phys.*, vol. 5, pp. 883–838, 1975.
[53] M. Bernasconi, G. L. Chiarotti, and E. Tosatti, "Ab initio calculations of structural and electronic properties of gallium solid-state phases," *Phys. Rev. B*, vol. 52, pp. 9988–9998, 1995.
[54] X. G. Gong, G. L. Chiarotti, M. Parrinello, and E. Tosatti, "α-gallium: a metallic molecular crystal," *Phys. Rev. B*, vol. 43, pp. 14277–14280, 1991.
[55] M. W. Knight, T. Coenen, Y. Yang, et al., "Gallium plasmonics: deep subwavelength spectroscopic imaging of single and interacting gallium nanoparticles," *ACS Nano*, vol. 9, pp. 2049–2060, 2015.
[56] J. Toudert and R. Serna, "Ultraviolet-visible interband plasmonics with p-block elements," *Opt. Mater. Express*, vol. 6, p. 2434, 2016.
[57] Y. Gutiérrez, M. Losurdo, P. García-Fernández, et al., "Dielectric function and plasmonic behavior of Ga (II) and Ga (III)," *Opt. Mater. Express*, vol. 9, pp. 4050–4060, 2019.
[58] X. F. Li, G. T. Fei, X. M. Chen, et al., "Size-temperature phase diagram of gallium," *EPL*, vol. 94, p. 16001, 2011.
[59] M. Yarema, M. Wörle, M. D. Rossell, et al., "Monodisperse colloidal gallium nanoparticles: synthesis, low temperature crystallization, surface plasmon resonance and Li-ion storage," *J. Am. Chem. Soc.*, vol. 136, pp. 12422–12430, 2014.
[60] X. Zhang, Q. Xu, L. Xia, et al., "Terahertz surface plasmonic waves: a review," *Adv. Photonics*, vol. 2, p. 1, 2020.
[61] P. Kuhne, N. Armakavicius, V. Stanishev, C. M. Herzinger, M. Schubert, and V. Darakchieva, "Advanced terahertz frequency-domain ellipsometry instrumentation for in situ and ex situ applications," *IEEE Trans. Terahertz Sci. Technol.*, vol. 8, pp. 257–270, 2018.
[62] J. B. Pendry, L. Martín-Moreno, and F. J. Garcia-Vidal, "Mimicking surface plasmons with structured surfaces," *Science (80-)*, vol. 305, pp. 847–848, 2004.
[63] J. Gómez Rivas, C. Schotsch, P. Haring Bolivar, and H. Kurz, "Enhanced transmission of THz radiation through subwavelength holes," *Phys. Rev. B*, vol. 68, p. 201306, 2003.
[64] E. Hendry, M. J. Lockyear, J. Gómez Rivas, L. Kuipers, and M. Bonn, "Ultrafast optical switching of the THz transmission through metallic subwavelength hole arrays," *Phys. Rev. B*, vol. 75, p. 235305, 2007.

[65] S. Pandey, B. Gupta, A. Chanana, and A. Nahata, "Non-drude like behaviour of metals in the terahertz spectral range," *Adv. Phys. X*, vol. 1, pp. 176–193, 2016.
[66] A. Lalisse, G. Tessier, J. Plain, and G. Baffou, "Quantifying the efficiency of plasmonic materials for near-field enhancement and photothermal conversion," *J. Phys. Chem. C*, vol. 119, pp. 25518–25528, 2015.
[67] P. C. Wu, C. G. Khoury, T.-H. Kim, et al., "Demonstration of surface-enhanced Raman scattering by tunable, plasmonic gallium nanoparticles," *J. Am. Chem. Soc.*, vol. 131, pp. 12032–12033, 2009.
[68] P. Albella, M. A. Poyli, M. K. Schmidt, et al., "Low-loss electric and magnetic field-enhanced spectroscopy with subwavelength silicon dimers," *J. Phys. Chem. C*, vol. 117, pp. 13573–13584, 2013.
[69] A. V. Krasavin, A. V. Zayats, and N. I. Zheludev, "Active control of surface plasmon–polariton waves," *J. Opt. A Pure Appl. Opt.*, vol. 7, pp. S85–S89, 2005.
[70] K. Shibuya, Y. Atsumi, T. Yoshida, Y. Sakakibara, M. Mori, and A. Sawa, "Silicon waveguide optical modulator driven by metal–insulator transition of vanadium dioxide cladding layer," *Opt. Express*, vol. 27, p. 4147, 2019.
[71] G. Sciaini, M. Harb, S. G. Kruglik, et al., "Electronic acceleration of atomic motions and disordering in bismuth," *Nature*, vol. 458, pp. 56–59, 2009.
[72] A. Cavalleri, C. Tóth, C. W. Siders, et al., "Femtosecond structural dynamics in VO_2 during an ultrafast solid-solid phase transition," *Phys. Rev. Lett.*, vol. 87, p. 237401, 2001.
[73] N. Yamada, E. Ohno, K. Nishiuchi, N. Akahira, and M. Takao, "Rapid-phase transitions of GeTe-Sb_2Te_3 pseudobinary amorphous thin films for an optical disk memory," *J. Appl. Phys.*, vol. 69, pp. 2849–2856, 1991.
[74] K. Nozaki, A. Lacraz, A. Shinya, et al., "All-optical switching for 10-Gb/s packet data by using an ultralow-power optical bistability of photonic-crystal nanocavities," *Opt. Express*, vol. 23, p. 30379, 2015.
[75] K. S. Novoselov, A. K. Geim, S. V. Morozov, et al., "Electric field effect in atomically thin carbon films," *Science*, vol. 306, pp. 666–669, 2004.
[76] V. Kochat, A. Samanta, Y. Zhang, et al., "Atomically thin gallium layers from solid-melt exfoliation," *Sci. Adv.*, vol. 4, pp. 1–12, 2018.
[77] Y. Li, J. Zhang, F. Yin, et al., "Ultra-thin Ga nanosheets: analogues of high pressure Ga(III)," *Nanoscale*, vol. 11, pp. 17201–17205, 2019.
[78] S. V. Badalov, M. Yagmurcukardes, F. M. Peeters, and H. Sahin, "Enhanced stability of single-layer w-gallenene through hydrogenation," *J. Phys. Chem. C*, vol. 122, pp. 28302–28309, 2018.
[79] D. Z. Metin, L. Hammerschmidt, and N. Gaston, "How robust is the metallicity of two dimensional gallium?," *Phys. Chem. Chem. Phys.*, pp. 27668–27674, 2018, https://doi.org/10.1039/c8cp05280h.
[80] J. P. Perdew, K. Burke, and M. Ernzerhof, "Generalized gradient approximation made simple," *Phys. Rev. Lett.*, vol. 77, pp. 3865–3868, 1996.
[81] J. P. Perdew, A. Ruzsinszky, G. I. Csonka, et al., "Restoring the density-gradient expansion for exchange in solids and surfaces," *Phys. Rev. Lett.*, vol. 100, p. 136406, 2008.
[82] Z. Wu and R. E. Cohen, "More accurate generalized gradient approximation for solids," *Phys. Rev. B*, vol. 73, p. 235116, 2006.
[83] J. M. Soler, E. Artacho, and J. D. Gale, "The SIESTA method for ab initio order-N materials simulation," *J. Phys. Condens. Matter.*, vol. 12, no. 11, 2002, https://doi.org/10.1088/0953-8984/14/11/302.
[84] Y. Li and T. F. Heinz, "Two-dimensional models for the optical response of thin films," *2D Mater.*, vol. 5, 2018, Art no. 025021.
[85] S. Choi, T.-H. Kim, H. O. Everitt, et al., "Kinetics of gallium adlayer adsorption/desorption on polar and nonpolar GaN surfaces," *J. Vac. Sci. Technol. B Microelectron. Nanometer Struct.*, vol. 25, p. 969, 2007.
[86] K. G. Steenbergen and N. Gaston, "Thickness dependent thermal stability of 2D gallenene," *Chem. Commun.*, vol. 55, pp. 8872–8875, 2019.

Supplementary Material: Supplementary material to this article can be found online at https://doi.org/10.1515/nanoph-2020-0314.